Journal of Geophysical Research: Solid Earth

RESEARCH ARTICLE
10.1029/2018JB015676

Investigating the Onset of Strain Localization Within Anisotropic Shale Using Digital Volume Correlation of Time-Resolved X-Ray Microtomography Images

Jessica McBeck[1], Maya Kobchenko[1], Stephen A. Hall[2], Erika Tudisco[3], Benoit Cordonnier[1,4], Paul Meakin[5], and François Renard[1,6]

[1]Physics of Geological Processes, The Njord Centre, Department of Geosciences, University of Oslo, Oslo, Norway, [2]Division of Solid Mechanics, Department of Construction Sciences, Lund University, Lund, Sweden, [3]Division of Geotechnical Engineering, Department of Construction Sciences, Lund University, Lund, Sweden, [4]The European Synchrotron Radiation Facility, Grenoble, France, [5]Department of Physics, Temple University, Philadelphia, PA, USA, [6]Université Grenoble Alpes, Université Savoie Mont Blanc, CNRS, IRD, IFSTTAR, ISTerre, Grenoble, France

Abstract Digital volume correlation analysis of time-resolved X-ray microtomography scans acquired during in situ triaxial compression of Green River shale cores provided time series of 3-D incremental strain fields that elucidated evolving deformation processes by quantifying microscopic strain localization. With these data, we investigated the impact of mechanical anisotropy on microscopic strain localization culminating in macroscopic shear failure. We conducted triaxial compression experiments with the maximum compressive stress, σ_1, aligned perpendicular and parallel to lamination planes in order to investigate end-member stress states that arise within sedimentary basins. When the preexisting laminations were perpendicular to σ_1, a lamination-parallel region with high axial compaction developed within the macroscopically linear deformation phase of the experiment and then thickened with increasing applied differential stress. Scanning electron microscopy images indicate that this axial compaction occurred within a lower density lamination and that more axial compaction occurred within the center of the core than near its sides. Boundary element method simulations suggest that this compacting volume promoted shear fracture development within the upper portion of the shale. When the laminations were parallel to σ_1, lamination-parallel dilation bands formed, thickened, and intensified in dilation. Population densities of the distributions of incremental shear strain, radial dilation, and axial contraction calculated by digital volume correlation analysis enabled quantification of the evolving overall impact of, and interplay between, these various deformation modes.

Key Points:
- Time-resolved in situ X-ray tomography imaging captured the path to macroscopic shear failure within shale
- Lamination-parallel zones of high incremental axial contraction and radial dilation developed prior to macroscopic failure
- Digital volume correlation and numerical modeling results suggest that axial compaction promoted shear strain localization

Supporting Information:
- Supporting Information S1
- Movie S1
- Movie S2
- Movie S3
- Movie S4
- Movie S5
- Movie S6
- Movie S7
- Movie S8
- Movie S9
- Movie S10
- Movie S11
- Movie S12
- Movie S13
- Movie S14
- Movie S15
- Movie S16

Correspondence to:
J. McBeck,
j.a.mcbeck@geo.uio.no

Citation:
McBeck, J., Kobchenko, M., Hall, S. A., Tudisco, E., Cordonnier, B., Meakin, P., & Renard, F. (2018). Investigating the onset of strain localization within anisotropic shale using digital volume correlation of time-resolved X-ray microtomography images. *Journal of Geophysical Research: Solid Earth*, *123*, 7509–7528. https://doi.org/10.1029/2018JB015676

Received 20 FEB 2018
Accepted 27 AUG 2018
Accepted article online 31 AUG 2018
Published online 17 SEP 2018

1. Introduction

Rocks contain fractures that may propagate stably until their local stress fields begin to interact. Stress interactions of multiple fractures may promote unstable propagation and lead to macroscopic failure (e.g., Ashby & Hallam, 1986). The conditions under which coalescing fractures transition from stable to unstable growth influence when fractures will propagate and failure will occur. Understanding the processes that control these conditions is critical for a wide variety of geoscience and engineering applications. In particular, the impact of fracture development within shale reservoirs on oil and gas production remains poorly understood (e.g., Gale et al., 2014). The rates of production in these reservoirs often exceed those expected from the low-permeability host shale, indicating that natural fracture development can increase hydrocarbon productivity within shale formations (e.g., Gale et al., 2014). This evidence suggests that fracture development can impact hydrocarbon productivity. However, the key characteristics of in situ natural fractures, such as size and shape distribution, hydraulic conductivity, and spatial connectedness, are difficult to determine, and so their impacts on hydrocarbon production remain poorly constrained.

Advances in time-resolved three-dimensional microtomography imaging (e.g., Renard et al., 2016, 2017) and three-dimensional digital volume correlation (DVC) analysis (e.g., Tudisco et al., 2017) enable in situ investigations of deformation processes via quantification of shear and volumetric strains within rocks and other materials. In this study, we aim to better understand fracture development within mechanically anisotropic

shale and characterize the transition from diffuse deformation to strain localization and the propagation of and slip along shear fractures. Accordingly, we measured time series of three-dimensional incremental strain fields from the onset of triaxial compressional loading to macroscopic shear failure. Previous experimental analyses have only inferred how damage evolves and localizes from acoustic emissions (e.g., Lockner et al., 1992), from the sizes and geometries of fractures visible on exposed surfaces (e.g., Wong & Einstein, 2009), and from elastic wave measurements (e.g., Sviridov et al., 2017). To investigate how preexisting mechanical anisotropy controls strain localization culminating in macroscopic shear failure, we calculated three-dimensional incremental strain fields from X-ray microtomograms acquired during two experiments using DVC analysis. We applied increasing axial compression either perpendicular or parallel to lamination bedding planes to capture end-member conditions that arise within sedimentary basins at depths of about 1 km. We focused on Green River shale because it has been studied extensively as a potential energy source (e.g., Lewan & Roy, 2011). Moreover, Green River shale is characteristic of organic-rich rocks that may be important in the natural carbon cycle and sequestration of CO_2 and hazardous waste.

2. Background

2.1. Macroscopic Shear Failure via Microscopic Fracture Coalescence

Microstructures near natural faults (e.g., Vermilye & Scholz, 1998) and fractures produced in laboratory experiments (e.g., Scholz, 1968) indicate that faults propagate through the interaction and coalescence of fractures. The failure mode, fracture network geometry, and stress field influence the critical stress required to initiate fracture growth (e.g., Clifton et al., 1976). Laboratory experiments provide insights into the evolving geometry of microscopic, interacting fractures that produce macroscopic failure (e.g., Reches & Lockner, 1994). Moment tensor analysis of acoustic emissions indicates that tensile failure dominates fracture initiation, but both shear and mixed-mode failure occur as fractures propagate and coalesce (Chang & Lee, 2004).

Laboratory experiments, numerical approaches, and field data provide further insights into how macroscopic failure occurs through the interaction and coalescence of fractures. Experiments that track visible fracture propagation on exposed surfaces indicate that fracture coalescence occurs through the propagation of tensile wing cracks that initiate at an angle to a preexisting fracture and through secondary shear fractures that propagate within their own plane (e.g., Park & Bobet, 2009; Sagong & Bobet, 2002; Shen et al., 1995; Wong et al., 2001; Wong & Einstein, 2009). Numerical approaches provide further insights into the conditions under which a few fractures coalesce into throughgoing shear fractures (e.g., Lee & Jeon, 2011; Madden et al., 2017; Tang et al., 2001). However, in intact crustal materials, inelastic yielding via fracture coalescence likely begins with many thousands of interacting fractures, pores, and other sources of mechanical heterogeneity that concentrate stresses rather than the tens of fractures with high length to width aspect ratios that are often investigated in laboratory experiments and numerical simulations. Experiments and numerical models that capture fracture interactions among only a few preexisting fractures likely capture an intermediate stage in the progression from intact rock to macroscopic failure (i.e., after some fracture coalescence has occurred, and the growth and coalescence of a relatively small number of large fractures dominates the path toward failure) but not the onset of yielding in crustal materials. Furthermore, during this intermediate stage, large fractures propagate through damaged material that already has a significant density of small fractures, and so the coalescence of small fractures may play an important role in the propagation of large fractures. Consequently, we focus on strain localization and the path to failure within rocks that are initially macroscopically intact.

In addition, although analytic solutions based on linear elastic fracture mechanics have been successfully used to predict the conditions under which stable growth and macroscopic failure occur (e.g., Donath, 1961), these formulations cannot fully describe the evolving physics within the process zone near a propagating fracture tip where inelastic deformation occurs within a high density of relatively small tensile fractures (e.g., Scholz, 1968; Vermilye & Scholz, 1998). Predicting how the interactions between many fractures lead to strain localization and control fault propagation remains an open area of research (e.g., Hoek & Martin, 2014).

2.2. Mechanical Anisotropy of Shales

We investigated the deformation and ultimate failure of initially intact Green River shale cores. In organic-rich shales, preexisting mechanical weaknesses, such as highly anisometric kerogen grains, laminations, and

planar clay-grain fabrics, likely control the locations at which fractures initiate and how they grow and coalesce in shales (e.g., Lash & Engelder, 2005). Laboratory experiments on rocks with natural mechanical weaknesses, such as bedding, cleavage, and schistosity, demonstrate that the uniaxial compressive strength can vary by more than 50% as the orientation of the weaknesses changes with respect to the maximum compressive stress (e.g., Donath, 1961). Recent shear wave splitting analyses provide further evidence of mechanical anisotropy within natural crustal shale, including shear wave triplication (Baird et al., 2017).

Both the stress field and the evolving fracture network geometry influence the anisotropy of the strength (e.g., Sarout & Guéguen, 2008) and the elasticity (e.g., Sviridov et al., 2017) of deforming shales. Higher lithostatic stresses tend to reduce porosity, which increases the uniaxial compressive strength (e.g., Donath, 1961) and compressional wave velocity (e.g., Dewhurst & Siggins, 2006; Melendez-Martinez & Schmitt, 2016; Ong et al., 2016; Sarout & Guéguen, 2008; Zadeh et al., 2016). Consequently, elastic wave velocity measurements have been used to infer the geometries of evolving porosity and fracture networks in shales (e.g., Baird et al., 2017). In addition to elastic velocities, permeability and capillary pressure fields evolve as external loading modifies the pore space, fracture apertures, and fracture connectivity. Consequently, understanding how evolving fracture geometry influences permeability and capillary pressure (e.g., Kwon et al., 2001) is critical for robust predictions of fluid flow and pressure diffusion in shale reservoirs for geotechnical applications such as CO_2 sequestration and hydrocarbon recovery.

3. Methods

3.1. Time-Resolved X-Ray Tomography of In Situ Triaxial Compression

We acquired three-dimensional tomograms of rock samples during their deformation in the HADES triaxial deformation apparatus installed on microtomography beamline ID19 at the European Synchrotron Radiation Facility (Renard et al., 2016). This deformation apparatus has low X-ray attenuation for energies $>$60 keV. It can capture 3-D snapshots of deformation within 2-min intervals as samples are loaded. The apparatus can apply axial and radial stresses up to 200 MPa, at temperatures up to 200 °C, with and without pore fluids.

In the reported experiments, we initially applied an isotropic confining pressure of 20 MPa to the samples, after which we increased the axial stress, σ_1, from 20 MPa, in increments of 2 MPa, with the confining stress held constant ($\sigma_2 = \sigma_3 = 20$ MPa), until the sample underwent macroscopic shear failure. We triaxially compressed the cores under 20-MPa confining stress in order to simulate the conditions within the shallow crust. This confining stress enabled strain localization and macroscopic shear failure to occur before reaching the axial stress limit of the deformation apparatus (200 MPa). We conducted the experiments at 25 °C, without pore fluid pressure. After each stress increment, we acquired X-ray attenuation data of the sample inside the rig with an acquisition time of less than 90 s. The combined time of scan acquisition and loading increase resulted in an average loading rate of approximately 2 MPa/5 min. Tomographic reconstruction of the acquired attenuation data provided three-dimensional maps of the linear attenuation coefficient consisting of cubic voxels with 6.5-μm side lengths (Figure 1 and Movies S1 and S2 in the supporting information). At this X-ray energy ($>$60 keV), the attenuation coefficient is an approximately linear function of material density.

For the present experiments, we cut cores from a block of organic-rich (R-8 unit) Green River shale that has been previously characterized and analyzed (Kobchenko et al., 2011; Panahi et al., 2013). This unit includes lacustrine marl/silt sediments that form mechanically anisotropic laminations with an average of 9.9 wt % organic matter (e.g., Kobchenko et al., 2011). The block had been equilibrating with the laboratory atmosphere for several years. Two cylindrical samples, with heights of 10 mm and diameters of 5 mm, were cored from this block with their major axes aligned approximately either perpendicular or parallel to the plane of the laminations within the shale. We employed great care in coring these anisotropic rocks and were able to achieve subparallel orientations with at most 10° between the maximum compression direction and lamination planes and subperpendicular orientations with even less deviation from the desired orientation. These laminations are varves produced by annual cycles of deposition. In the experiments, we imposed the maximum compressive stress, σ_1, in the direction of the major axes of the cylinders (vertical). The cores were not dried before the experiments, and there was no humidity control in the beamline. We did not lubricate the faces of the shale cores that were in contact with the apparatus pistons that applied the axial load.

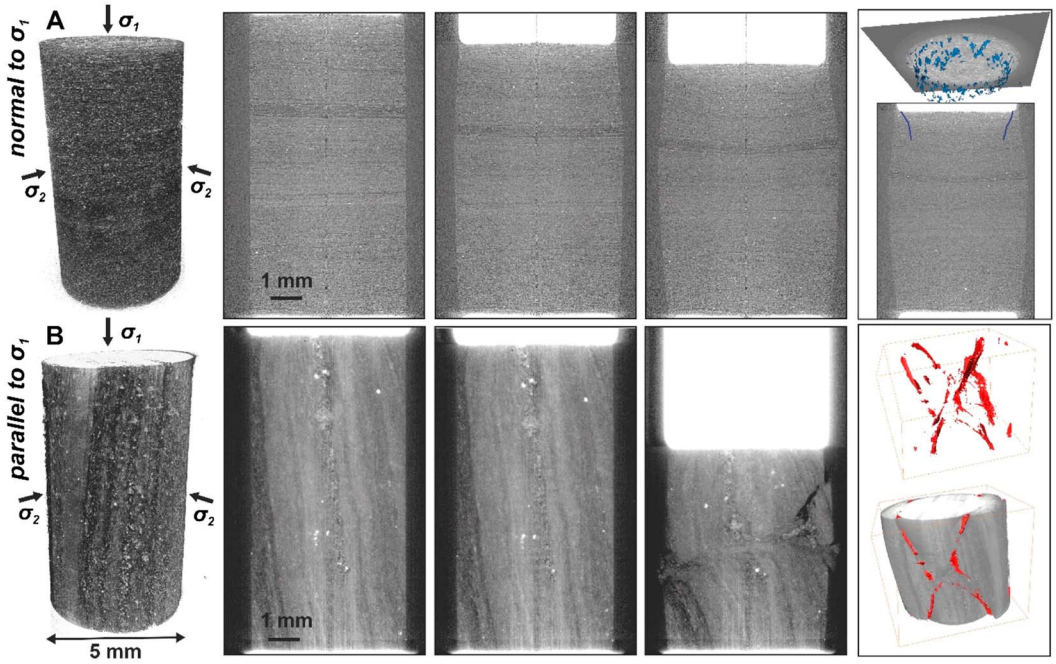

Figure 1. Volumes and vertical cross sections of tomography scans acquired during the experiment with laminations normal (a) and parallel (b) to σ_1, with increasing applied differential stress from left to right. The column on the right shows low density volumes in blue and red identified via thresholding and interpreted as fractures in the tomogram acquired after macroscopic shear failure. Thresholding of the tomograms' grayscale values extracts volumes with lower density than the surrounding host rock. Dilated fractures produce local decreases in density, and so these lower density volumes are interpreted as fractures. The downward moving white rectangle at the top of each image is the upper piston, which has a higher X-ray attenuation coefficient than the shale.

Lower density regions observed within the three-dimensional tomographic images indicate the presence of pores and fractures. Therefore, we could detect the initiation, growth, and coalescence of fractures if they had apertures greater than about half the voxel size (3.2 μm in these experiments) and thereby caused a sufficient change in the local attenuation coefficient (e.g., Renard et al., 2017). The attenuation coefficient of the solid organic matter within Green River shale (mainly kerogen) is larger than that of the gas-filled pores and fractures but smaller than that of the inorganic minerals. The volumes, orientations, and shapes of most of the solid organic matter particles do not change substantially during deformation and failure. Consequently, with image segmentation we could successfully distinguish dilatational fractures from strongly anisometric kerogen particles.

3.2. DVC Analysis

The fine grain size and low initial porosity of the Green River shale hinder the direct detection of developing fractures from the X-ray attenuation reconstructions, except in the final tomograms acquired after macroscopic shear failure (Figure 1). Consequently, DVC analysis was critical in quantifying deformation preceding macroscopic failure in these shale experiments. We used the software TomoWarp2 (Tudisco et al., 2017) to execute the DVC analysis. TomoWarp2 finds the translations and rotations that best map subvolumes within one three-dimensional image onto subvolumes in another image by identifying similar patterns within these subvolumes (Hall, 2006, Hall et al., 2010; Tudisco et al., 2017, 2015). The size of these subvolumes depends on parameters of the calculation set by the user and in particular the correlation window size. The subvolumes are distributed over a regular grid that covers the sample area in the tomography scans with a user-defined node spacing.

We performed three independent DVC analyses on each experiment. First, we calculated the three-dimensional incremental displacement fields between pairs of microtomography scans that were separated by approximately equal changes in macroscopic axial strain, $\varepsilon^{M}_{zz'}$ (0.01–0.02) throughout the total duration of

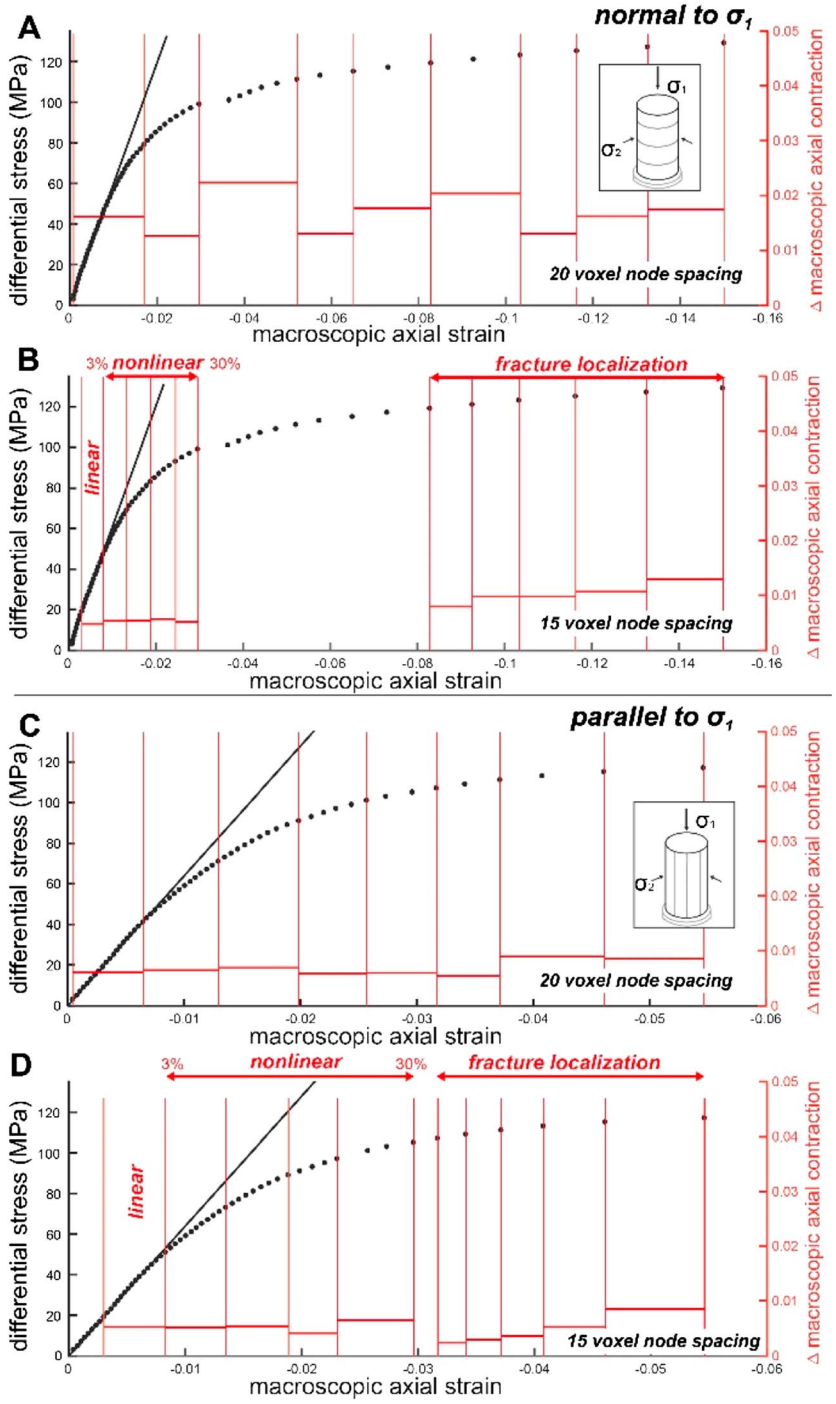

Figure 2. Loading history of experiment with laminations normal (a, b) and parallel (c, d) to σ_1. Black dots show the differential stress and macroscopic axial strain after each increment of σ_D at which we acquired a tomogram. Black lines show linear regressions through the early portions of the stress-strain data. Red vertical lines show the set of tomograms used in each DVC analysis. Red horizontal lines show the magnitude of $\Delta\varepsilon_{zz}^{M}$ between each set of tomograms. (a, c) Scans used in DVC analyses with 20 voxel node spacing that encompass each complete experiment. (b, d) Scans used in DVC analyses with 15 voxel node spacing that capture the phases of nonlinear deformation and fracture localization. DVC = digital volume correlation.

both experiments using a DVC node spacing of 20 voxels (Figure 2). We calculated ε_{zz}^{M} from the change in length of each sample relative to its initial length observed in the microtomography scans. In the two other DVC analyses, we used higher temporal resolution (i.e., smaller macroscopic stress increments) and

higher spatial resolution to focus on two stages of particular interest: (1) when the shale began to deviate from macroscopic linear behavior to nonlinear behavior and (2) over the final five stress increments as shear fractures began to localize and propagate. In each of these analysis, the change in the macroscopic axial strain between each pair of analyzed tomograms was constrained by the difficulty of producing accurate displacement fields when the deformation produced by a particular differential stress increase was large and by the increasing noise in the displacement fields when deformation was small.

Throughout both experiments, the macroscopic mechanical behavior transitioned gradually from the early linear deformation phase, in which there was an approximately linear relationship between macroscopic strain and stress, to deviation from linear deformation to nonlinear deformation behavior and finally to macroscopic shear failure. For the purposes of these DVC analyses, we defined the nonlinear deformation phase to begin when the difference between the measured ε_{zz}^{M} and the strain predicted from extrapolation of the linear portion of the experiment was 3% and to end when that difference was 30% of the measured ε_{zz}^{M}. Accordingly, the first increment of this DVC analysis included only macroscopically linear stress-strain behavior, and the second increment began when the difference between the measured and predicted ε_{zz}^{M} was 3% of the measured ε_{zz}^{M} (Figure 2). The final increment ended when that difference was 30% of the measured ε_{zz}^{M} (Figure 2). Each of the analyzed pairs of scans was separated by an approximately equal change in ε_{zz}^{M} (0.05–0.07).

To investigate shear fracture localization leading to macroscopic shear failure, we calculated incremental strain fields over the last five increments of differential stress increase in each experiment. In this analysis, 2 MPa of differential stress increase separates each pair of tomograms, and the increasing deviation from linear macroscopic stress-strain behavior produced increasing differences in $\Delta\varepsilon_{zz}^{M}$ between each pair of tomograms (Figure 2). The incremental strain fields obtained from the three DVC analyses reveal strain localization that occurred within the time (stress) interval between the acquisitions of the pair of microtomography scans rather than the cumulative strain from the onset of loading.

Following tests of the influence of the correlation window size and node spacing on the resolution, computation time, and robustness of the resulting displacement fields, we selected a correlation window size of ±10 voxels and node spacing size of 15 or 20 voxels. We used the larger node spacing size (20 voxels) in DVC analyses that encompass each complete experiment, and we used the smaller node spacing size (15 voxels) in the other two DVC analyses. These parameter choices provide a compromise between computational efficiency, spatial resolution, and robustness. The node spacing size can influence the magnitude of the displacements that TomoWarp2 calculates. With larger node spacing, generally lower strains are calculated due to averaging displacement gradients over larger volumes. The magnitude of the errors produced in DVC analyses depends on the choice of parameters used in the analysis as well as the quality of the tomograms. Consequently, constraining the potential magnitude of error in the calculated displacement fields remains difficult to determine in a general fashion.

3.3. Characterization of DVC Strain Fields

To quantitatively characterize the deformation of the shale, we calculated components of the Green Lagrangian strain tensor field from the displacement fields determined by the DVC analysis. We describe the incremental axial contraction and radial dilation using the incremental axial normal strain, $\partial\varepsilon_{zz}$, and the sum of the incremental strains that are perpendicular to σ_1, $\partial\varepsilon_{xx} + \partial\varepsilon_{yy}$, respectively. To characterize the incremental shear strain, we calculate the von Mises yield criterion equivalent strain, $(3J_2)^{1/2}$, where J_2 is the second invariant of the strain deviator tensor, $J_2 = \frac{1}{3}I_1{}^2 - I_2$, and I_1 and I_2 are the first and second invariants of the strain tensor calculated in the DVC analysis. In this coordinate system, the *z* axis is vertical (parallel to σ_1) and *x*-*y* plane is horizontal (perpendicular to σ_1). We consider dilatational strain as positive and contractive strain as negative. As the shale cores shortened axially and thickened radially (Figure 1 and Movies S1 and S2), we expect the axial strain to become increasingly negative with increasing contraction, the radial strain components to increase with increasing dilation, and the von Mises yield criterion strain to increase with increasing shear strain.

To ensure robust comparison of the magnitude of the incremental strain tensor components between experimental increments, we divided each incremental strain value by the absolute change in ε_{zz}^{M} that occurred

between the selected tomography scans. We do not expect that $\Delta\varepsilon_{zz}^{M}$ will produce exactly proportional changes in all of the components of the incremental strain tensor but that higher $\Delta\varepsilon_{zz}^{M}$ will be correlated with higher incremental strains. Because we divided each component by the absolute value of $\Delta\varepsilon_{zz}^{M}$, the signs of the incremental strain components or invariants remain unchanged.

To characterize the incremental strain fields, we first calculated the median projections of each 3-D strain field, in which we found the medians of $\frac{\partial\varepsilon_{zz}}{\Delta\varepsilon_{zz}^{M}}$, $\frac{\partial\varepsilon_{xx}+\partial\varepsilon_{yy}}{\Delta\varepsilon_{zz}^{M}}$, and $\frac{\partial(3J_2)^{1/2}}{\Delta\varepsilon_{zz}^{M}}$ along a certain direction, (the *x* axis or *y* axis direction) over a 2-D grid (the *y*-*z* plane or *x*-*z* plane). Then we quantified the evolving incremental strain by constructing histograms of the values of $\frac{\partial\varepsilon_{zz}}{\Delta\varepsilon_{zz}^{M}}$, $\frac{\partial\varepsilon_{xx}+\partial\varepsilon_{yy}}{\Delta\varepsilon_{zz}^{M}}$, and $\frac{\partial(3J_2)^{1/2}}{\Delta\varepsilon_{zz}^{M}}$, for each of the three DVC analyses. We normalized each histogram by the number of points at which the incremental strain was calculated, so each histogram shows the probability of finding strain values within certain ranges. Next, in order to understand how the most common parts of the population densities evolved as the shale approached macroscopic failure, we found the ranges of $\frac{\partial\varepsilon_{zz}}{\Delta\varepsilon_{zz}^{M}}$, $\frac{\partial\varepsilon_{xx}+\partial\varepsilon_{yy}}{\Delta\varepsilon_{zz}^{M}}$, and $\frac{\partial(3J_2)^{1/2}}{\Delta\varepsilon_{zz}^{M}}$ that were between their 40th and 60th percentile values.

3.4. Scanning Electron Microscopy

To better characterize the microscopic deformation that led to macroscopic shear failure in both of the experiments, we analyzed vertical cross sections of the shale with scanning electron microscopy (SEM). After macroscopic failure of each shale core in the in situ triaxial tests, we impregnated the cores with epoxy to prevent ex situ damage. We then cut the cores along a midsection vertical plane, polished the newly exposed surface, and coated the surface with 8 nm of carbon. We imaged the exposed surfaces using a Hitachi S2500 Scanning Electron Microscope (SEM) at the University of Grenoble with a voltage of 16 kV and a Hitachi SU5000 SEM at the University of Oslo with a voltage of 15 kV. The results from each microscope are sufficiently similar to compare for our purposes.

3.5. Boundary Element Method Numerical Modeling

To investigate the impact of compaction on shear localization, we used the two-dimensional, plane strain, linear elastic boundary element method code Fric2D (Cooke & Pollard, 1997), which is available as part of the GROW package tools on GitHub. Fric2D solves the quasi-static equations of deformation to determine the displacements and tractions on each element at specified points within the model that are produced by a given set of boundary conditions and fracture geometries (e.g., Cooke & Pollard, 1997). Boundaries and fractures are discretized into linear segments that may translate, rotate, open, or slip in response to tractions or displacements applied to the boundaries or perturbations from other fractures. With this quasi-static approach, intact material between boundaries and fractures behaves as a linear elastic material, and the model determines the equilibrium stress and strain fields within the host material after each incremental change of the boundaries, as well as opening, closing, and slip along fractures. By changing the normal stiffness of a fracture element, the two sides of each element are allowed to cross each other. Consequently, Fric2D can capture local shear, dilation, and contraction that contributes to nonlinear macroscopic behavior.

In the present study, we hypothesize that in the experiment with laminations perpendicular to σ_1, localized axial compaction along a horizontal lamination promoted shear strain localization near the upper surface of the shale core. To test this hypothesis, we used Fric2D to simulate a vertical cross section of the experiment over the loading increment during which we observed this shift in the pattern of shear strain localization from the bottom to the top portion of the core (Figures 3 and 8). Accordingly, we built numerical models in which the height and width match the dimensions of the shale core within this experimental loading increment. We applied 20 MPa of compressional stress to the left and right sides of the model, matching the experimental confining stress, and allowed these sides to move up and down without experiencing shear tractions (τ = 0 MPa), thereby allowing downward movement of the top side. The application of 20 MPa of confining stress did not significantly change the width of the model, so the dimensions of the model preceding axial loading are similar to the dimensions of the shale core preceding confining stress loading. We kept the bottom boundary fixed with no normal or shear displacements ($u_n = u_s = 0$ mm). We applied normal displacement to the top boundary of the model that matches the displacement of the top piston that occurred within the experiment increment (u_n = 0.13 mm) and prevented this boundary from moving laterally (u_s = 0 mm).

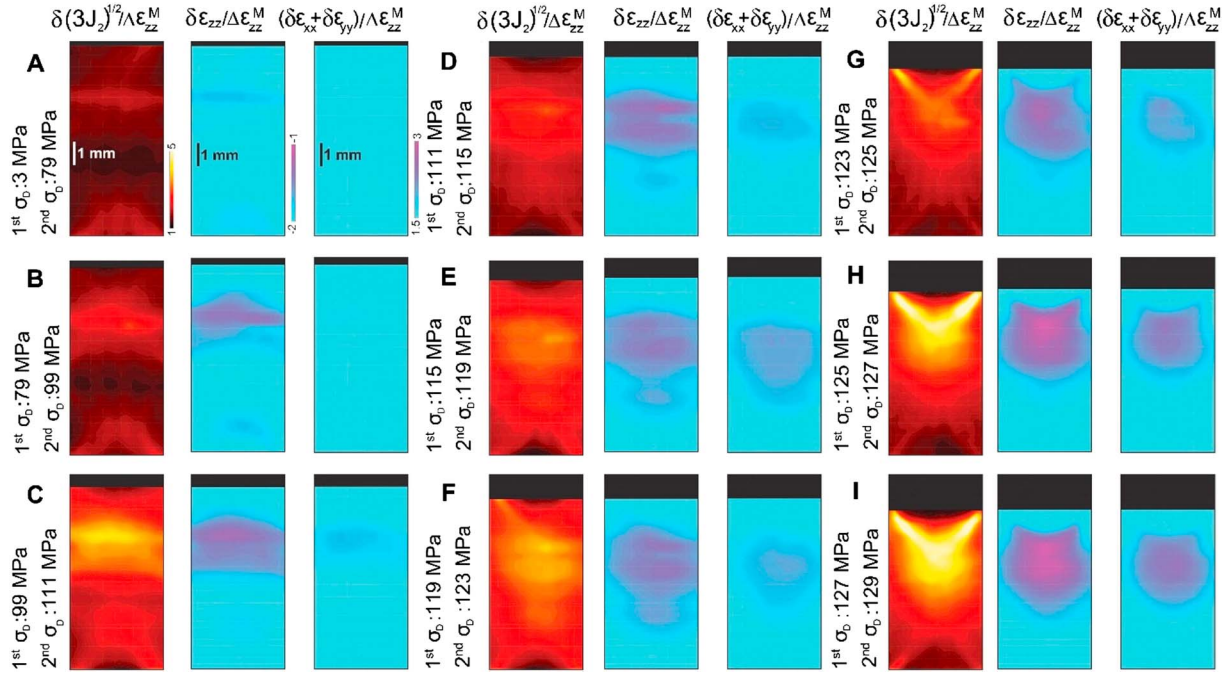

Figure 3. (a–i) Median projections in the *x* direction of the normalized incremental strain during the experiment with laminations perpendicular to σ_1 obtained from digital volume correlation analysis with 20 voxel node spacing. Movie S4 shows the median projections in the *y* direction. The first, second, and third columns show $\frac{\partial(3J_2)^{1/2}}{\Delta\varepsilon_{zz}^M}$, $\frac{\partial\varepsilon_{zz}}{\Delta\varepsilon_{zz}^M}$, and $\frac{\partial\varepsilon_{xx}+\partial\varepsilon_{yy}}{\Delta\varepsilon_{zz}^M}$, respectively. Contraction is negative.

We prevented the top and bottom boundaries of the model from moving laterally because the shale-piston interfaces were not lubricated in the experiments. The DVC fields do not show large horizontal displacements within the shale near the shale-piston interface during the modeled experiment increment. However, the shear tractions on these surfaces were not negligible as the friction between the shale core and the pistons suppressed sliding. Consequently, a fixed lateral displacement boundary condition (u_s = 0 mm) captures the stress state at the piston interfaces better than a shear traction-free boundary condition. We monotonically increased the normal displacement applied to the top boundary in 10 steps, while we applied constant confining pressure to the side walls in order to match the loading evolution in the experiments.

In this linear elastic model, we prescribed a Young's modulus of 200 MPa and a Poisson's ratio of 0.25. We calculated the Young's modulus from the experimental stress-strain data (Figures 2a and 2b) acquired from the onset of the nonlinear deformation phase (σ_D = 110 MPa) until just before macroscopic failure (σ_D = 131 MPa) $\left(\frac{131\text{ MPa}-110\text{ MPa}}{0.150-0.044}\approx 200\text{ MPa}\right)$. We calculated the Young's modulus from the later portion of the experiment rather than the earlier quasilinear portion because during the simulated increment (σ_D = 123–125 MPa) distributed damage had already reduced the stiffness of the rock matrix throughout the shale core, as well as through the development of a compacting lamination subperpendicular to σ_1. Although the magnitude of the macroscopic strain increased superlinearly with increasing axial stress in this phase of the experiment, the 200-MPa Young's modulus obtained from the experimental data enables the numerical models to produce strain fields similar to those produced in the experiments.

In Fric2D, the length of the boundary and fracture elements should be greater than or equal to 2 times the amount by which they are displaced in order to satisfy the small strain assumption of Eulerian deformation. We used an element length of 0.26 mm to enable our models to remain numerically robust when we displaced the top side by 0.13 mm. The confining pressure applied to the side walls caused a displacement of the elements by an order of magnitude less than an element length. Thus, an element length of 0.26 mm was the smallest length that could be used to obtain a robust numerical solution. This element length provided an optimal compromise between stability and accuracy, which increases with decreasing element length.

To control the amount of axial compaction that occurred along the simulated compaction bands, we varied the element normal stiffness (K_n) of each element within three simulated bands. The amount by which a simulated band compacts depends on K_n, as well as the length of the simulated band, orientation of the band, and loading conditions. Consequently, the K_n parameter modulates the bulk elastic modulus of the model. The experimental DVC axial contraction fields revealed higher axial contraction within the upper central portion of the shale. Consequently, we varied K_n with an approximately parabolic distribution along each band so that the center portions compacted more than the portions closer to the model sides. In order to match the DVC fields, we also applied higher K_n to the lower bands so that they compacted less than the upper bands. Systematic tests with K_n distributions with varying ranges of K_n minima demonstrated that altering this minimum did not strongly impact the resulting distribution of shear strain as long as this minimum was low enough to allow compaction along the bands. As the K_n minimum decreased, the areas of high shear strain near the top corners spread further downward toward the compacting volumes.

The Green River shale is elastically anisotropic, and so an anisotropic stiffness tensor best describes its mechanical response (e.g., Chenevert & Gatlin, 1965). In Fric2D, only one Young's modulus and Poisson's ratio may be prescribed to the intact rock. However, introducing fracture elements that may compact allows the Young's modulus to vary throughout the model. If elements compact, then the local stiffness surrounding the compacting elements is lower than the stiffness prescribed to the intact rock. Although a two-dimensional linear elastic model that includes compacting elements may not be able to quantitatively match the deformation of three-dimensional nonlinear anisotropic rock, these simulations enabled qualitative comparison between the model results and experimental data and so provided insight into the interaction of volumetric and shear strain localization.

With these models, we aimed to address the simple question: How do compacting subplanar volumes impact the distribution of shear strain? Although we benefited from rich 3-D data, the planar nature of the laminations, symmetrical loading conditions, and symmetrical localizations of shear strain in the experiment with horizontal laminations enabled this question to be addressed robustly with 2-D models. Shear fracture development may break this symmetry, but we aimed to simulate shear strain localization and not the propagation of shear fractures. In the experiment with horizontal laminations, the localization of shear strain developed approximately radially symmetric, and so this 2-D model is more applicable than if the symmetry had been broken. The application of this linear elastic model to our fundamental question is reasonable because the onset of compaction band formation occurred before the macroscopic stress-strain response became strongly nonlinear in this experiment. In the differential stress range in which shear strain developed near the upper shale surface, the relationship between the macroscopic axial stress and axial strain was approximately linear.

4. Results

4.1. Macroscopic Stress-Strain Relationships

The macroscopic mechanical behavior of each shale core includes the following: (1) a quasilinear deformation phase in which each 2-MPa increment in differential stress, $\sigma_D = \sigma_1 - \sigma_2 = \sigma_1 - \sigma_3$, produced nearly equal changes in axial strain, (2) a nonlinear deformation phase in which successive 2-MPa increments of σ_D produced increasingly larger changes in axial strain, (3) a prefailure phase in which strain localized onto a few larger fractures, and (4) macroscopic shear failure (Figure 2). The stress at which the macroscopic axial strain differed by 10% from that predicted by extrapolation of the linear strain-stress relationship obtained by linear regression of the low differential stress data (σ_D = 3–40 MPa) occurred at nearly the same differential stress in both experiments (σ_D = 59 MPa). The differential stresses at which the measured axial contraction differs from the predicted axial contraction by 3% (47 and 51 MPa) and 30% (99 and 105 MPa), which delimit the nonlinear deformation phase analyzed with DVC, also occurred at nearly the same values in both experiments.

The mechanical behaviors of the shale cores of the two experiments differ in a few critical ways. The magnitude of the macroscopic axial strain immediately preceding macroscopic failure of the shale core with laminations perpendicular to σ_1 was almost 3 times larger (0.15) than that of the experiment with laminations parallel to σ_1 (0.055). In addition, the maximum differential stress achieved in the experiment with laminations perpendicular to σ_1 was 12 MPa higher (σ_D = 129 MPa) than in experiment with laminations parallel

to σ_1 (σ_D = 117 MPa). Additional experiments in the HADES deformation rig on two other shale cores with laminations set subparallel to σ_1, cut from the same block of Green River shale, and exhibited mechanical failure behavior similar to that reported here. For all three experiments with subparallel lamination orientations, the differential stresses immediately preceding failure were 119–120 MPa, and macroscopic axial strains immediately preceding failure were 0.055–0.057. The consistency of these values demonstrates that the observed differences between experiments with differing lamination orientations arose primarily from the differing lamination orientation rather than differing natural heterogeneity in one of the cores such as preexisting fractures or weaker laminations.

4.2. Incremental Strain Evolution

In the experiment with laminations perpendicular to σ_1, fields of the incremental axial strain, $\partial\varepsilon_{zz}$, divided by $\Delta\varepsilon_{zz}^{M}$, and the sum of the incremental strain components perpendicular to σ_1, $\partial\varepsilon_{xx} + \partial\varepsilon_{yy}$, divided by $\Delta\varepsilon_{zz}^{M}$, reveal a subhorizontal compaction band about 6 mm above the bottom piston of the deformation apparatus (Figure 3). In the following discussion, we focus on patterns in the incremental strain fields revealed in a median projection along one axis in the horizontal plane. The supporting information movies show projections along the perpendicular axis in the horizontal plane. The symmetry of the laminations and loading conditions produce only small differences in the patterns of the median projections of the strain fields before fractures begin to develop at the edges of the shale-piston interfaces, and so we concentrate on only one projection direction here. The subhorizontal compaction band appeared within the linear deformation phase of the experiment and became a zone of localized axial contraction and radial dilation as it grew in thickness away from the upper surface of the shale cylinder (Figure 3 and Movies S3 and S4). In particular, the band appeared in the first increment of the nonlinear deformation DVC analysis (between differential stresses of 19 and 47 MPa when the macroscopic stress-strain relationship transitioned from linear to nonlinear) and then thickened as the strain-stress relationship became increasingly nonlinear (Figures S1b–S1e and Movies S5 and S6).

Toward the end of the experiment, localized zones of the von Mises yield criterion equivalent strain, $\partial(3J_2)^{1/2}$, divided by $\Delta\varepsilon_{zz}^{M}$, became concentrated near the upper surface of the sample, and grew in length toward the subhorizontal compacting band (Figures 3g–3i and S1f–S1j and Movies S7 and S8). Early in the experiment, $\frac{\partial(3J_2)^{1/2}}{\Delta\varepsilon_{zz}^{M}}$ localized near both the upper and lower pistons but then increased in magnitude and extent near the upper piston. It is likely that these localizations of $\frac{\partial(3J_2)^{1/2}}{\Delta\varepsilon_{zz}^{M}}$ began to develop near the pistons because we did not lubricate the horizontal top and bottom faces of the shale core that were in contact with the pistons. This lack of lubrication provided frictional resistance against lateral movement of the shale core, which then localized shear strain near the edges of the upper and bottom core faces. The pattern of $\frac{\partial(3J_2)^{1/2}}{\Delta\varepsilon_{zz}^{M}}$ within the final DVC strain field, which captured strain within the last two increments of the experiment preceding macroscopic shear failure, closely matches the fracture geometry observed in the tomogram acquired after macroscopic shear failure (Figure 1).

After the differential stress exceeded 80% of the failure differential stress in the experiment with laminations parallel to σ_1 (σ_D = 97 MPa), the $\frac{\partial\varepsilon_{xx}+\partial\varepsilon_{yy}}{\Delta\varepsilon_{zz}^{M}}$ fields hosted subvertical concentrations of high dilation aligned along the orientation of preexisting laminations (Figures 4 and S2e and Movies S9–S12). Throughout loading, vertically oriented $\frac{\partial\varepsilon_{xx}+\partial\varepsilon_{yy}}{\Delta\varepsilon_{zz}^{M}}$ localizations accommodated increasing amounts of dilation, even as the change in macroscopic axial strain remained nearly constant. Furthermore, the $\frac{\partial(3J_2)^{1/2}}{\Delta\varepsilon_{zz}^{M}}$ field reveals that incremental shear strain began to concentrate near one side of the bottom core surface and then grew toward the center of the sample (Figure 4 and Movies S9–S12). The $\frac{\partial\varepsilon_{zz}}{\Delta\varepsilon_{zz}^{M}}$ and $\frac{\partial\varepsilon_{xx}+\partial\varepsilon_{yy}}{\Delta\varepsilon_{zz}^{M}}$ fields show that this region also hosted axial contraction and radial opening (Figures 4g and 4h and Movies S13 and S14). The overlapping localizations of high $\frac{\partial(3J_2)^{1/2}}{\Delta\varepsilon_{zz}^{M}}$, $\frac{\partial\varepsilon_{zz}}{\Delta\varepsilon_{zz}^{M}}$, and $\frac{\partial\varepsilon_{xx}+\partial\varepsilon_{yy}}{\Delta\varepsilon_{zz}^{M}}$ of the final calculated DVC increment partially match the fracture geometry extracted from the tomogram that was acquired after macroscopic shear failure (Figure 1). However, the strain fields do not show the core-spanning fractures observed in this tomogram because the final displacement fields obtained for DVC analysis related the last two tomograms preceding macroscopic shear failure, when the core-spanning fractures were not yet fully developed. The incremental strains between the tomograms acquired immediately preceding and after failure were too large to allow robust DVC analysis, so we

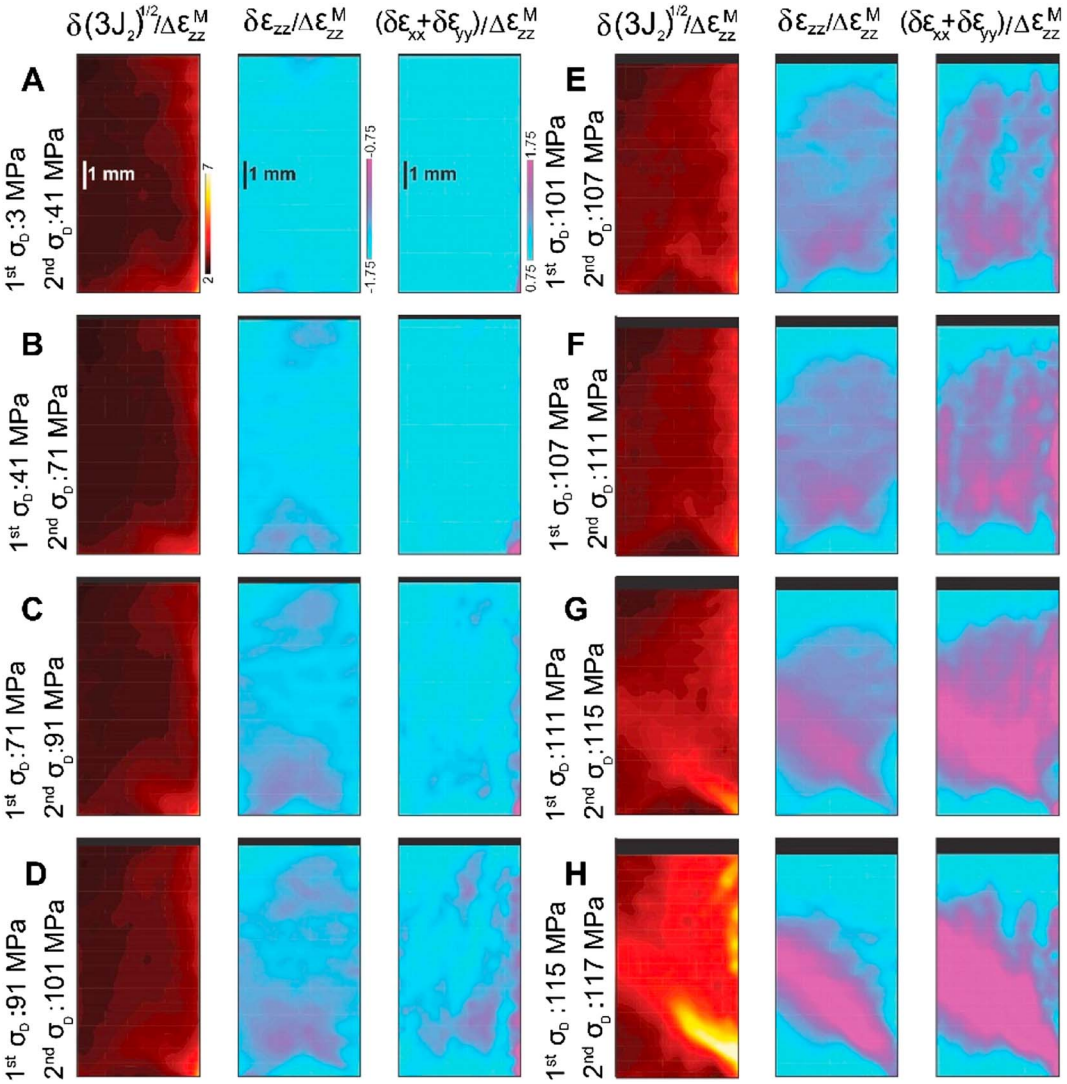

Figure 4. (a–h) Incremental strain evolution of experiment with laminations parallel to σ_1 obtained from digital volume correlation analysis with 20 voxel node spacing. The format is identical to that of Figure 3. Median projections in the other orientation are shown in Movie S9.

did not include this strain field in the analysis. In this study, we aim to understand the micromechanics preceding macroscopic failure rather than the physics during dynamic macroscopic failure. Consequently, we designed this experimental study to provide rich in situ detail about strain localization from the onset of loading until immediately preceding macroscopic failure rather than the deformation that occurs during dynamic failure.

To further test the robustness of the patterns observed in the incremental strain fields, we calculated the cumulative strain fields within the final five increments of both experiments at a DVC node spacing of 15 voxels (Figures S3 and S4 and Text S1). The patterns in the cumulative strain fields (Figures S3 and S4) are similar to those observed in the final incremental strain fields of each experiment (Figures S1 and S2). The supporting information describes the similarities of the patterns in more detail (Text S1).

The volumes that host the highest values of $\frac{\partial \varepsilon_{zz}}{\Delta \varepsilon_{zz}^{M}}$ in the final increment of each experiment have distinctly different shapes in the two experiments (Figure S5). In the experiment with laminations perpendicular to σ_1, the concentration of high $\frac{\partial \varepsilon_{zz}}{\Delta \varepsilon_{zz}^{M}}$ has a gumdrop shape when visualized in three dimensions and borders the U shape of the bottom boundary of a volume undergoing minimal axial contraction (Figure S5 and

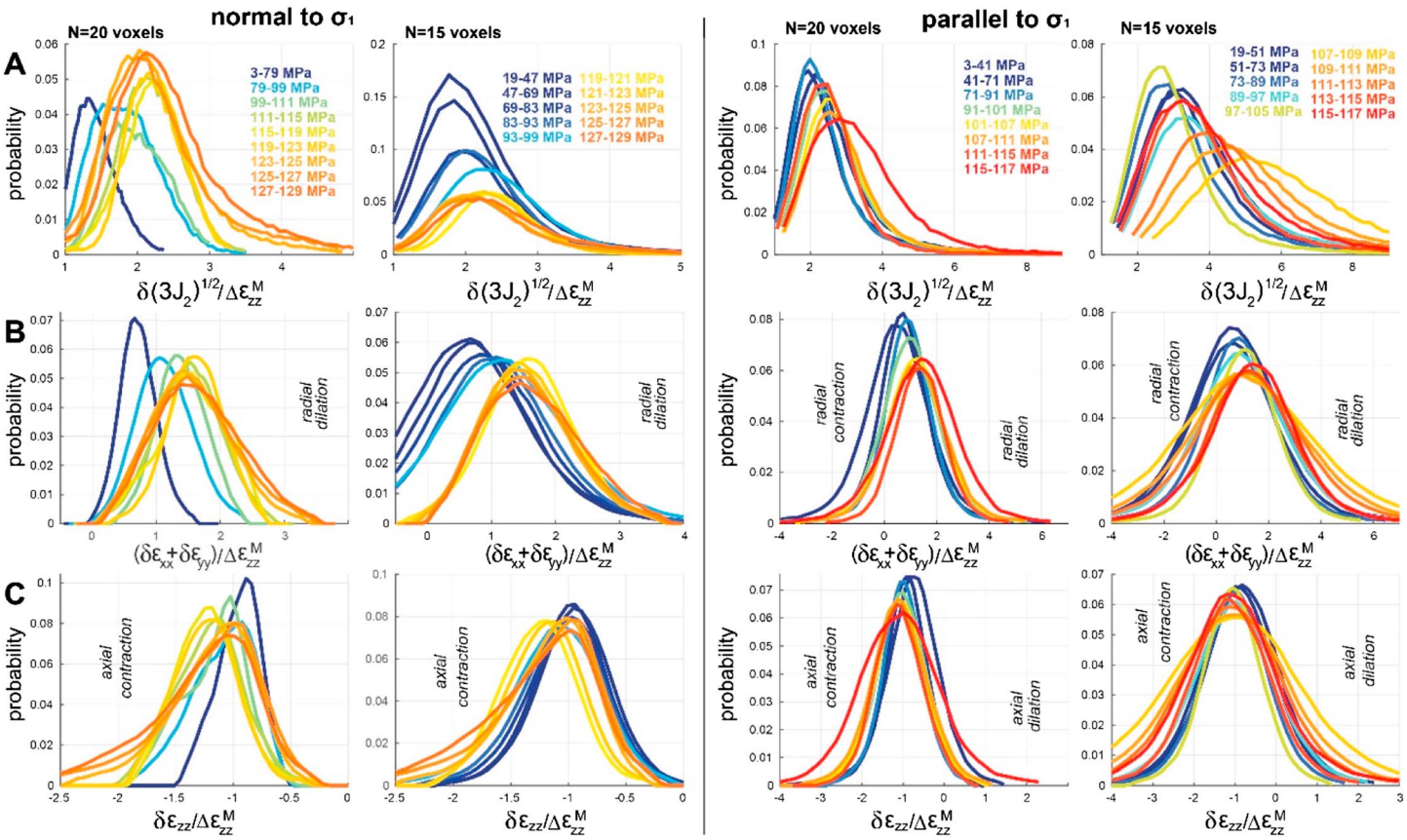

Figure 5. Histograms of components of the incremental strain tensor divided by $\Delta\varepsilon_{zz}^{M}$ for the experiment with laminations normal (first two columns) and parallel (last two columns) to σ_1. For each experiment, the first and second columns show histograms from the DVC analysis with 20 voxel node spacing ($N = 20$ voxels) and the 15 voxel node spacing ($N = 15$ voxels), respectively. (a–c) Histograms of $\frac{\partial(3J_2)^{1/2}}{\Delta\varepsilon_{zz}^{M}}$, $\frac{\partial\varepsilon_{xx}+\partial\varepsilon_{yy}}{\Delta\varepsilon_{zz}^{M}}$, and $\frac{\partial\varepsilon_{zz}}{\Delta\varepsilon_{zz}^{M}}$, respectively. The colors of the curves indicate the experimental increment and correlate to the text in the plots that list the differential stress of the first and second scans used in each digital volume correlation calculation.

Movie S15). In the experiment with laminations parallel to σ_1, the region of high $\frac{\partial\varepsilon_{zz}}{\Delta\varepsilon_{zz}^{M}}$ appears roughly planar in three dimensions, inclined at ~45°, and overlaps the region of high $\frac{\partial(3J_2)^{1/2}}{\Delta\varepsilon_{zz}^{M}}$ (Figure S5 and Movie S16).

4.3. Histograms of Strain Populations

To quantitatively describe the evolution of incremental strain, we report histograms of the $\frac{\partial(3J_2)^{1/2}}{\Delta\varepsilon_{zz}^{M}}$, $\frac{\partial\varepsilon_{zz}}{\Delta\varepsilon_{zz}^{M}}$, and $\frac{\partial\varepsilon_{xx}+\partial\varepsilon_{yy}}{\Delta\varepsilon_{zz}^{M}}$ populations in each increment from the three DVC analyses. In both experiments, the histograms of $\frac{\partial(3J_2)^{1/2}}{\Delta\varepsilon_{zz}^{M}}$ generally shifted toward larger values, higher positive skewness, and higher variance with increasing differential stress (Figure 5a). The growth of the high $\frac{\partial(3J_2)^{1/2}}{\Delta\varepsilon_{zz}^{M}}$ regions from the shale-piston interface toward the center of the core (Figures 3 and 4) produced these statistical changes. The histograms of $\frac{\partial\varepsilon_{xx}+\partial\varepsilon_{yy}}{\Delta\varepsilon_{zz}^{M}}$ shifted toward increasingly dilatational extremes (Figure 5b), and the $\frac{\partial\varepsilon_{zz}}{\Delta\varepsilon_{zz}^{M}}$ histograms shifted toward increasingly contractive values (Figure 5c). We observe this progression of increasing incremental axial contraction with increasing incremental radial dilation in these strain populations and also infer this evolution from the shortening and widening of the core observed in the microtomography images (Figure 1 and Movies S1 and S2) and the positive Poisson's ratio of most materials. The volumetric strain populations do not show as significant an increase in skewness and variance as the $\frac{\partial(3J_2)^{1/2}}{\Delta\varepsilon_{zz}^{M}}$ populations (Figure 5).

The highest density of the $\partial\varepsilon_{zz}$ populations for most of the increments of both experiments is close to the value of $\Delta\varepsilon_{zz}^{M}$, causing $\frac{\partial\varepsilon_{zz}}{\Delta\varepsilon_{zz}^{M}}$ to be approximately one (Figure 5c). In contrast, the highest population density

of the $\frac{\partial\varepsilon_{xx}+\partial\varepsilon_{yy}}{\Delta\varepsilon_{zz}^{M}}$ populations is not close to 2, indicating that the most common magnitude of radial dilation does not approach the magnitude of macroscopic axial contraction for each experiment increment. These results are consistent with estimates of the Poisson's ratio for Green River shale (0.2; e.g., Aadnoy & Looyeh, 2011).

Although the evolutions of $\frac{\partial(3J_2)^{1/2}}{\Delta\varepsilon_{zz}^{M}}$ and $\frac{\partial\varepsilon_{zz}}{\Delta\varepsilon_{zz}^{M}}$ are similar in both experiments, the evolution of $\frac{\partial\varepsilon_{xx}+\partial\varepsilon_{yy}}{\Delta\varepsilon_{zz}^{M}}$ differs between the experiments. In the experiment with laminations perpendicular to σ_1, only 1–4% of the local $\frac{\partial\varepsilon_{xx}+\partial\varepsilon_{yy}}{\Delta\varepsilon_{zz}^{M}}$ values from the analysis that encompasses the full experiment were contractive (negative), whereas 20–30% of the $\frac{\partial\varepsilon_{xx}+\partial\varepsilon_{yy}}{\Delta\varepsilon_{zz}^{M}}$ values were contractive in the experiment with laminations parallel to σ_1. These contractive portions of the radial strain population were concentrated between the vertical zones of high radial dilation (Figures 4e–4h). A higher percentage of radial contraction may have occurred in the experiment with laminations parallel to σ_1 relative to the other experiment because when the laminations were parallel to σ_1, layer-perpendicular opening likely promoted radial dilation along the lamination contacts, which then produced radial contraction within the laminations. In the experiment with laminations parallel to σ_1, layer-perpendicular normal strain occurred only as axial compaction and not radial dilation. Because tensile failure along the lamination contacts likely occurred under lower differential stress than other failure modes within other portions of the shale (i.e., shear failure within the layers), the orientation of these weak mechanical contacts with respect to the stress field was the primary control of strain localization by either promoting or hindering opening of lamination contacts or within weak laminations.

The histograms from the analyses with 15 voxel node spacing that encompass the onset of nonlinear deformation are broader than the first two increments of the 20 voxel node spacing analysis, which cover the same differential stress range. The supporting information describes how both the node spacing and $\Delta\varepsilon_{zz}^{M}$ contribute to noise in the DVC displacement fields (Text S2).

4.4. Strain Population Densities

To further characterize the evolution of strain localization and, in particular, the values that have the highest population density of the incremental strain components, we report the median (50th percentile) values of $\frac{\partial(3J_2)^{1/2}}{\Delta\varepsilon_{zz}^{M}}$, $\frac{\partial\varepsilon_{zz}}{\Delta\varepsilon_{zz}^{M}}$, and $\frac{\partial\varepsilon_{xx}+\partial\varepsilon_{yy}}{\Delta\varepsilon_{zz}^{M}}$ as functions of σ_D (Figure 6). To capture variations in the highest population density values at each experiment increment, we also show the 40th and 60th percentile values of each population.

In both experiments, the median of the $\frac{\partial(3J_2)^{1/2}}{\Delta\varepsilon_{zz}^{M}}$ population generally shifted toward larger values with increasing σ_D for the DVC analysis using 20 voxel node spacing (Figure 6a). However, in the DVC analyses with 15 voxel node spacing, the median of $\frac{\partial(3J_2)^{1/2}}{\Delta\varepsilon_{zz}^{M}}$, as well as the ranges between the 40th and 60th percentiles, remained relatively constant or decreased approaching failure. These differing evolutions suggest that the median of the $\frac{\partial(3J_2)^{1/2}}{\Delta\varepsilon_{zz}^{M}}$ population is more sensitive to differences in the node spacing size than the medians of the other strain components.

In both experiments, the median of $\frac{\partial\varepsilon_{xx}+\partial\varepsilon_{yy}}{\Delta\varepsilon_{zz}^{M}}$ became increasingly dilatational (Figure 6b) while the median of $\frac{\partial\varepsilon_{zz}}{\Delta\varepsilon_{zz}^{M}}$ became increasingly contractive (Figure 6c). These trends were mostly consistent throughout the experiment with laminations parallel to σ_1, whereas in the final few increments of the other experiment, the range between the 40th and 60th percentiles remained at similar values. In the final three increments of the experiment with laminations perpendicular to σ_1, the median of $\frac{\partial(3J_2)^{1/2}}{\Delta\varepsilon_{zz}^{M}}$ continuously increased, whereas the median of $\frac{\partial\varepsilon_{xx}+\partial\varepsilon_{yy}}{\Delta\varepsilon_{zz}^{M}}$ and median of $\frac{\partial\varepsilon_{zz}}{\Delta\varepsilon_{zz}^{M}}$ achieved relatively stable states, signaling a potential limit to the incremental strain components, but not to the incremental shear strain, as the shale approached macroscopic shear failure.

4.5. SEM of Postfailure Microstructures

SEM images of axial cross sections of the shale cores following failure provide additional insights into the fracture geometries that led to macroscopic shear failure and how fracture propagation and slip modified the surrounding shale matrix (Figure 7). SEM images of the experiment with laminations perpendicular to σ_1

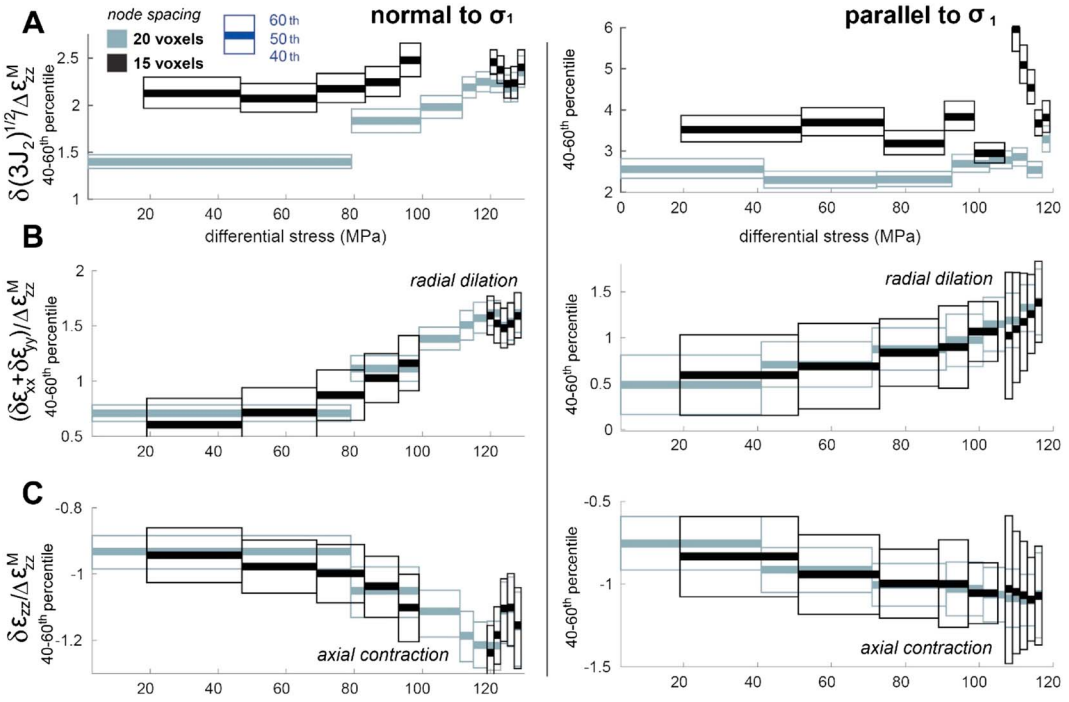

Figure 6. Characteristic values of (a) $\frac{\partial(3J_2)^{1/2}}{\Delta\varepsilon_{zz}^M}$, (b) $\frac{\partial\varepsilon_{xx}+\partial\varepsilon_{yy}}{\Delta\varepsilon_{zz}^M}$, and (c) $\frac{\partial\varepsilon_{zz}}{\Delta\varepsilon_{zz}^M}$ for experiment with laminations normal (first column) and parallel (second column) to σ_1 as a function of the differential stress. The thickest horizontal lines show median (50th percentile) values, and the upper and lower thinner horizontal lines show the 40th and 60th percentile values. Gray and black boxes show results from digital volume correlation analyses using 20 voxel node spacing and 15 voxel node spacing, respectively.

show evidence of a prominent darker colored (lower density) horizontal lamination (Figure 7a, white arrow). The DVC strain fields indicate that compaction nucleated near this lamination in the linear deformation phase and subsequently accommodated incremental axial contraction (Figures 3 and S1). In the SEM images, the width of the band appears larger toward the edge of the shale core than in the center of the core, indicating that the center portion of the band compacted by a greater degree than the portions of the band near the edges. In addition, in this experiment, shear fractures propagated by breaking through the laminations and entraining grains in a narrow slip zone (Figure 7b). In the experiment with laminations parallel to σ_1, the fracture zones appear wider (Figures 7c and 7d) than in the other experiment. However, unloading of the sample may have contributed to these larger widths. These SEM images also reveal dilation along the laminations, bending of the initially vertical laminations toward the fractures, and compaction and grain size reduction within the fracture slip zone (Figure 7d).

4.6. Insights From Numerical Modeling

Early in the experiment with laminations perpendicular to σ_1, high shear strain, $\frac{\partial(3J_2)^{1/2}}{\Delta\varepsilon_{zz}^M}$, concentrated near the bottom and top core piston interfaces and then high $\frac{\partial(3J_2)^{1/2}}{\Delta\varepsilon_{zz}^M}$ concentrated near the upper surface while $\frac{\partial(3J_2)^{1/2}}{\Delta\varepsilon_{zz}^M}$ remained low near the lower face (Movie S15 and Figures 3 and 8a). We hypothesize that the presence of the axially compacting volume in the upper portion of the shale core promoted shear strain localization near the upper shale core surface. To test this hypothesis, we used the two-dimensional plane strain boundary element method code Fric2D to simulate a vertical cross section of this experiment increment from σ_D = 123 to 125 MPa, which is the differential stress range at which we observed the shift of the higher $\frac{\partial(3J_2)^{1/2}}{\Delta\varepsilon_{zz}^M}$ zones from the lower to the upper portion of the shale core. Accordingly, we built numerical models that aim to match the shale core geometry, Young's modulus, applied confining stress, increase in the macroscopic axial strain, boundary conditions, and distribution of axial compaction observed within this experiment increment (Figure 8b). We varied the element normal stiffness (K_n) of each element within three simulated compaction

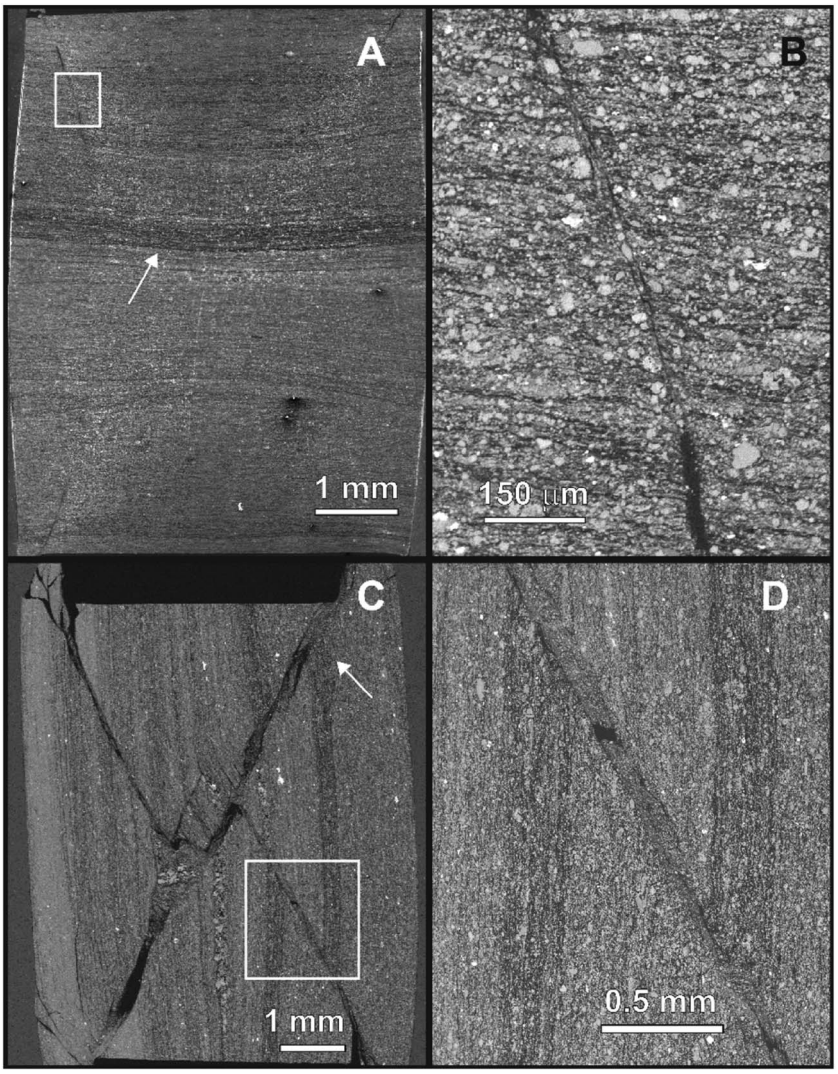

Figure 7. Scanning electron microscopy images of postfailure microstructures of experiment with laminations perpendicular (a, b) and parallel (c, d) to σ_1. Inset white box in (a) is shown in (b). Inset white box in (c) is shown in (d). (a) Darker colored lamination (white arrow) appears to be thinner near the center of the shale core than near its sides. (b) Grains are entrained in fracture. (c, d) Vertical laminations bend slightly and thicken toward shear fracture (white arrow).

bands to control the distribution of axial compaction (Figure 8) and so approximately match the axial contraction fields observed in the experiment (Figure 3). Other than K_n, the elements have identical property values.

When we excluded the compaction bands in the model, localizations of shear strain, ε_{xz}, developed at the corners (Figure 8c). These high shear strain zones developed because we prevented the top and bottom sides from moving laterally while we applied 20 MPa of confining stress to the left and right sides. These loading conditions caused the left and right sides to displace toward the model center while the top and bottom sides remained laterally fixed. When we included compaction bands in the numerical model (Figure 8), the high ε_{xz} zones in the upper corners grew toward the center and bottom of the model, but the high ε_{xz} zones near the lower corners remained unchanged. Comparison of the contours of the shear strain fields from models that exclude and include the simulated compaction bands indicates that the axial compaction, which concentrated within the darker colored lamination in the upper portion of the core (Figures 1a and 7a), promoted the growth of areas with high ε_{xz} near the upper portion but did not change the ε_{xz} distribution near the lower portion.

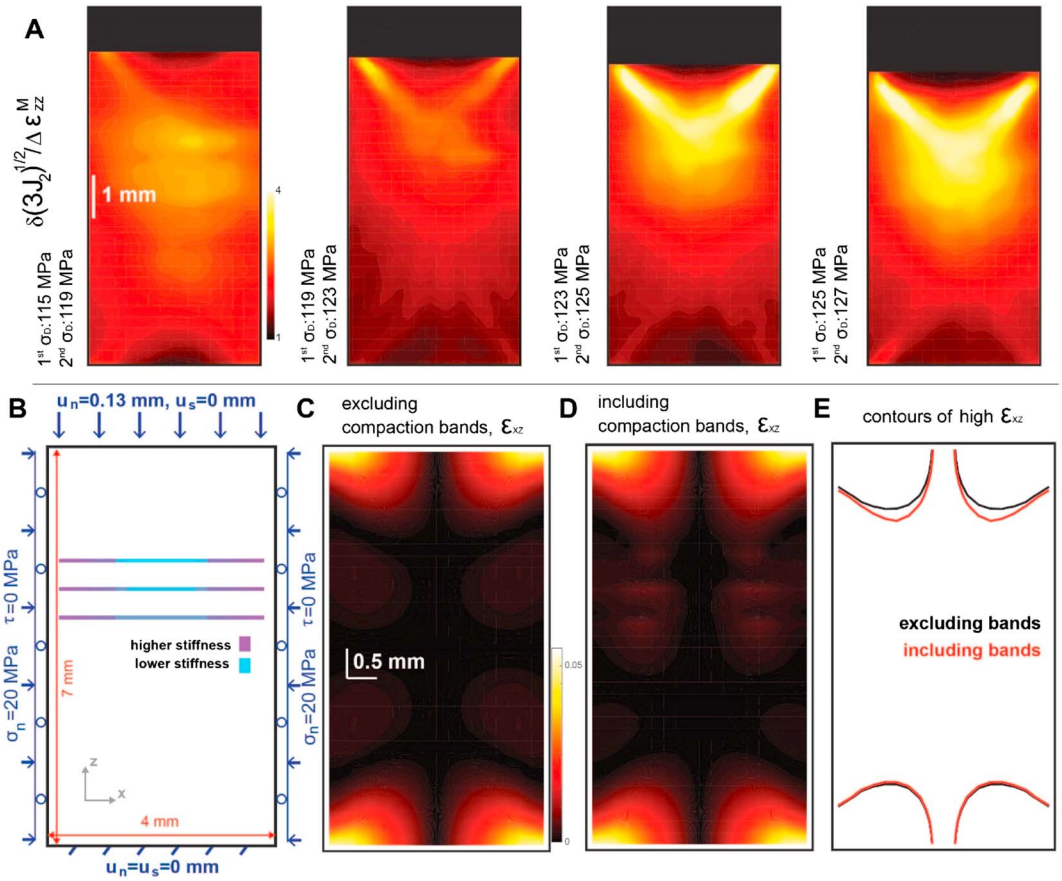

Figure 8. Numerical modeling to assess the impact of compaction bands on shear strain localization. (a) Median projections of $\frac{\partial(3J_2)^{1/2}}{\Delta\varepsilon_{zz}^{M}}$ from the experiment with laminations perpendicular to σ_1. (b) Setup of boundary element method models. (c) Shear strain, ε_{xz}, within 2-D numerical model without simulated compaction bands. (d) The ε_{xz} field with compaction bands. (e) Contour intervals of ε_{xz} from models excluding (black) and including (red) compaction bands. Compaction bands increased the area of the shale experiencing higher ε_{xz} (>0.006) near the top of the shale core.

5. Discussion

5.1. Influence of Mechanical Anisotropy on Strain Localization

In both experiments, the orientation of preexisting laminations impacted the distribution of radial dilation and axial compaction preceding macroscopic shear failure. Physical compaction orients clay and other minerals within shale and so produces compaction fabrics that contribute to elastic and strength anisotropy (e.g., Dewhurst et al., 2011; Heling, 1970). In the Green River shale cores studied here, annual deposition cycles built the laminations (varves), so variations of organic and inorganic mineralogy across lamination interfaces produced the strength anisotropy.

The incremental strain fields indicate that (1) in the experiment with the laminations parallel to σ_1, the vertical laminations concentrated radial dilation in vertical-trending lamination-parallel zones (Figure 4) and (2) in the experiment with the laminations perpendicular to σ_1, a subhorizontal, lamination-parallel volume enhanced compaction as well as radial dilation (Figure 3). The lamination-parallel vertical localizations of radial dilation observed in the experiment with laminations parallel to σ_1, and the lower differential stress at failure achieved in this experiment (117 MPa) relative to that of the other experiment (129 MPa), suggest that opening along laminations reduced the effective strength of the shale when the laminations were parallel to σ_1. When the laminations were perpendicular to σ_1, the stress field did not promote opening along the lamination contacts because fractures, and other quasi-planar zones of low axial stiffness, were under compression. Consequently, compaction within the laminations rather than lamination-parallel opening accommodated

axial strain, thereby increasing the effective strength relative to the other experiment and allowing greater macroscopic axial contraction to occur prior to macroscopic shear failure (Figure 2).

Fractures at high angles relative to bedding planes tend to be more widespread than fractures parallel to bedding within natural shale outcrops exposed at the surface (e.g., Gale et al., 2014). In particular, shear wave splitting analysis indicates strong elastic anisotropy (up to 30%) in the Horn River shale formation dominated by anisotropy with a vertical axis of symmetry, which is overprinted by anisotropy with a horizontal axis of symmetry (Baird et al., 2017). A vertical fracture set aligned parallel to σ_1 produces the anisotropy with a horizontal axis of symmetry, whereas layering and, potentially, some layer-parallel cracks produce the anisotropy with a vertical axis of symmetry (Baird et al., 2017). Bedding-perpendicular fractures suggest that the least compressive stress was aligned parallel to the bedding planes when the fractures formed (e.g., Narr & Suppe, 1991). We captured this state in the experiment with laminations perpendicular to σ_1. In this experiment, we observed layer-perpendicular (axial) compaction, as well as layer-parallel (radial) dilation (Figure 3 and Movies S3–S8). These DVC analysis results indicate that in sedimentary basins, layer-parallel dilation may produce discrete fractures orientated subnormal to bedding, and layer-perpendicular compaction may produce compaction fabrics aligned parallel to bedding.

In sedimentary basins undergoing horizontal compression, the strain fields observed in the experiment with laminations parallel to σ_1 are more likely to arise than those observed in the other experiment. When laminations or other mechanical anisotropies are parallel to σ_1 and buried at a depth of about 1 km (23-MPa lithostatic compression with 2,300-kg/m^3 density rock), the DVC analysis indicates that lamination-perpendicular dilation may lead to opening-mode failure along those lamination interfaces (Figure 4 and Movies S9–S14). Dewhurst et al. (2011) also identified tensile fractures aligned parallel to bedding within a shale core plug and attribute their formation to planes of weakness within the bedding plane. Observations from exposed shale outcrops have identified bedding-parallel fractures between bedding laminations or planar fabrics (Gale et al., 2014). Such bedding-parallel fractures may be influenced by unloading during natural crustal exhumation. However, this DVC analysis provides in situ evidence of dilation along bedding-parallel planes.

The boundary conditions of the shale cores in the HADES triaxial compression experiments do not exactly match those acting on shale cores embedded within a kilometer-scale volume of shale, even if they are subjected to the same principal stresses. We must consider the impact of experimental boundary effects on deformation when extrapolating laboratory results to crustal environments. In these experiments, the interfaces of the shale core in contact with the pistons were not lubricated. The DVC analysis reveals that the edges of these interfaces appear to localize shear strain and subsequently nucleate shear fractures near shale-piston interfaces, indicating that boundary effects influenced the development the shear fractures. However, these effects did not appear to influence the location or geometry of the vertical lamination-parallel dilation zones or the horizontal lamination-parallel contraction zone. Rather, the orientation of the laminations had a more significant impact on these strain concentrations than the boundary effects.

Although field observations provide constraints on the impact of mechanical anisotropy on macroscopic failure, and the microtomograms captured cumulative dilatational fracture development within this shale in the final experiment increments, the DVC analyses captured the development of localizing incremental volumetric and shear strain. The resulting strain fields enabled quantification of the evolving deformation, including the interplay between incremental volumetric and shear strain, as the shale approached macroscopic failure.

5.2. Interaction of Volumetric and Shear Deformation

Our analysis suggests that localization of volumetric strains promotes the concentration of shear strain into regions with greater volumetric strain than neighboring volumes. In the experiment with laminations perpendicular to σ_1, contraction localized within a subhorizontal band near the top of the core that thickened downward (Figure 3). Initially, shear strain developed near both the upper and lower surfaces of the cores, but as the compacting volume grew, shear strain became increasingly concentrated near the upper core face and subsequently grew toward the compacting volume (Figure 3). Numerical simulations of an increment of this experiment suggest that a compacting volume in the upper portion of the core promoted shear strain growth in the upper portion but did not influence the shear strain field in the lower portion (Figure 8). Similarly, in the experiment with laminations parallel to σ_1, shear strain localized and grew outward from

the lower shale-piston interface toward a volume of the core that accommodated higher axial contraction and radial dilation than other regions (Figure 4). In addition, the evolution of the incremental strain values with the highest population density (Figure 6) revealed that the rate of strain accumulation as a function of differential stress did not consistently increase as the shale approached macroscopic shear failure. Furthermore, this rate differed between the incremental volumetric and shear strain components, as well as between each experiment. As strain localized onto proto-fractures in the final increment of both experiments, the most common values of the shear strain field continually increased, whereas the most common values of the volumetric strain fields did not substantially change (Figure 6). The DVC analysis demonstrates that fractures that manifested macroscopically as shear fractures developed through a variety of smaller-scale failure mechanisms ranging from purely shear to purely volumetric. In addition, this analysis indicates that the interaction of tensile, compressional, and shear deformation contributes to strain localization from the onset of deformation to macroscopic shear failure.

Previous analyses of deformation band development provide ample evidence for the promotion of shear strain localization via volumetric deformation in porous sedimentary rocks (e.g., Aydin & Johnson, 1983), similar to that observed in our analysis. Whereas throughgoing faults form via microcrack coalescence in low porosity rocks (e.g., Reches & Lockner, 1994), in high porosity rocks, and sediments, faults may develop from the failure of preexisting deformation bands (e.g., Aydin & Johnson, 1978). Deformation bands are generally tabular, millimeter to centimeter thick volumes with higher cohesion and stiffness that can accommodate localized compaction and shear (e.g., Fossen et al., 2007). These relatively rigid and strong tabular aggregates can concentrate stresses and become nucleation sites for shear fractures, consistent with observations from the DVC analyses and numerical models. In addition, in Rothbach sandstone, the degree to which compaction localizes into discrete bands, or remains diffuse, depends on the existence and orientation of bedding planes (e.g., Louis et al., 2007). Our results indicate that shear strain localization is promoted in regions that have experienced higher volumetric strains, likely due to corresponding stress concentrations, which arise due to the orientation of preexisting laminations. Although the link between stress-concentrating deformation bands and discrete shear fractures is well recognized in sandstones (e.g., Louis et al., 2007), our DVC analysis provides in situ evidence of volumetric strain promoting shear strain localization within shale.

6. Conclusions

DVC analysis of time-resolved microtomography scans of laminated Green River shale cores acquired during triaxial compression tests indicates that the orientation of mechanical weaknesses influences strain localization preceding macroscopic shear failure. The impact of the laminations on the three-dimensional incremental strain fields became apparent after the differential stress reached 35% of the differential stress at failure in both experiments as lamination-parallel dilatational zones in the experiment with laminations parallel to σ_1 (Figure 4) and as a lamination-parallel compaction zone in the experiment with laminations perpendicular to σ_1 (Figure 3). The SEM images reveal that this compaction zone developed within a lower density lamination that accommodated more axial compaction within the center of the shale core than toward the sides (Figure 7). The orientation of the laminations influenced the magnitude of the peak failure stress by concentrating stresses and strains along lamination-parallel weaknesses. The maximum differential stress preceding macroscopic shear failure is lower in the experiment with laminations parallel to σ_1 than in the experiment with laminations parallel to σ_1 (Figure 2), likely because the lamination orientation promoted layer-perpendicular opening (tensile-dominated failure) in this configuration. The DVC analysis of time-resolved microtomography scans enabled quantification of the spectrum of microscopic failure modes that contributed to fracture development, demonstrating that microscopic opening, closing, and shearing acted in concert to produce macroscopic shear failure.

Acknowledgments
The deformation apparatus was built by Sanchez Technology. Elodie Boller, Paul Tafforeau, and Alexander Rack provided advice on the design of the tomography setup. This study received funding from the Norwegian Research Council (project HADES, grant 250661). B. C. was funded by the European Union's Horizon 2020 Research and Innovation Programme under the ERC Advanced Grant Agreement 669972, *Disequilibrium Metamorphism* (*DIME*). Beamtime was allocated at the European Synchrotron Radiation Facility (Long Term Proposal ES-295). Data storage was provided by UNINETT Sigma2—the National Infrastructure for High Performance Computing and Data Storage in Norway (project NS9073K). The X-ray tomography data (series of 3-D volumes, 16-bytes gray scale) supporting the conclusions can be downloaded at Renard, F., McBeck, J. (2018). https://doi.org/10.11582/2018.00005. Fric2D is available as part of the GROW package tools on GitHub (https://github.com/mlcooke/GROW). We thank Editor Douglas Schmitt and two anonymous reviewers who helped us to improve this work.

References

Aadnoy, B., & Looyeh, R. (2011). *Petroleum rock mechanics: Drilling operations and well design*. The Boulevard Langford Lane, Oxford: Gulf Professional Publishing (imprint of Elsevier). OX5. ISBN: 978-0-12-385546-6

Ashby, M. F. A., & Hallam, S. D. (1986). The failure of brittle solids containing small cracks under compressive stress states. *Acta Metallurgica*, *34*(3), 497–510. https://doi.org/10.1016/0001-6160(86)90086-6

Aydin, A., & Johnson, A. (1978). Development of faults as zones of deformation bands and as slip surfaces in sandstone. *Pure and Applied Geophysics*, *116*(4-5), 931–942. https://doi.org/10.1007/BF00876547

Aydin, A., & Johnson, A. M. (1983). Analysis of faulting in porous sandstones. *Journal of Structural Geology*, *5*(1), 19–31. https://doi.org/10.1016/0191-8141(83)90004-4

Baird, A. F., Kendall, J.-M., Fisher, Q. J., & Budge, J. (2017). The role of texture, cracks, and fractures in highly anisotropic shales. *Journal of Geophysical Research: Solid Earth*, *122*, 10,341–10,351. https://doi.org/10.1002/2017JB014710

Chang, S., & Lee, C. (2004). Estimation of cracking and damage mechanisms in rock under triaxial compression by moment tensor analysis of acoustic emission. *International Journal of Rock Mechanics and Mining Sciences*, *41*(7), 1069–1086. https://doi.org/10.1016/j.ijrmms.2004.04.006

Chenevert, M. E., & Gatlin, C. (1965). Mechanical anisotropies of laminated sedimentary rocks. *Society of Petroleum Engineers Journal*, *5*(01), 67–77. https://doi.org/10.2118/890-PA

Clifton, R. J., Simonson, E. R., Jones, A. H., & Green, S. J. (1976). Determination of the critical-stress-intensity factor K Ic from internally pressurized thick-walled vessels. *Experimental Mechanics*, *16*(6), 233–238. https://doi.org/10.1007/BF02329274

Cooke, M. L., & Pollard, D. (1997). Bedding-plane slip in initial stages of fault-related folding. *Journal of Structural Geology*, *19*(3-4), 567–581. https://doi.org/10.1016/S0191-8141(96)00097-1

Dewhurst, D. N., & Siggins, A. F. (2006). Impact of fabric, microcracks and stress field on shale anisotropy. *Geophysical Journal International*, *165*(1), 135–148. https://doi.org/10.1111/j.1365-246X.2006.02834.x

Dewhurst, D. N., Siggins, A. F., Sarout, J., Raven, M. D., & Nordgård-Bolås, H. M. (2011). Geomechanical and ultrasonic characterization of a Norwegian Sea shale. *Geophysics*, *76*(3), WA101–WA111. https://doi.org/10.1190/1.3569599

Donath, F. A. (1961). Experimental study of shear failure in anisotropic rocks. *Geological Society of America Bulletin*, *72*(6), 985–989. https://doi.org/10.1130/0016-7606(1961)72[985:ESOSFI]2.0.CO;2

Fossen, H., Schultz, R., Shipton, Z., & Mair, K. (2007). Deformation bands in sandstone: A review. *Journal of the Geological Society*, *164*(4), 755–769. https://doi.org/10.1144/0016-76492006-036

Gale, J. F., Laubach, S. E., Olson, J. E., Eichhubl, P., & Fall, A. (2014). Natural fractures in shale: A review and new observations. *AAPG Bulletin*, *98*(11), 2165–2216. https://doi.org/10.1306/08121413151

Hall, S. A. (2006). A methodology for 7D warping and deformation monitoring using time-lapse seismic data. *Geophysics*, *71*(4), O21–O31.

Hall, S. A., Bornert, M., Desrues, J., Pannier, Y., Lenoir, N., Viggiani, G., & Bésuelle, P. (2010). Discrete and continuum analysis of localised deformation in sand using X-ray μCT and volumetric digital image correlation. *Géotechnique*, *60*(5), 315–322. https://doi.org/10.1680/geot.2010.60.5.315

Heling, D. (1970). Micro-fabrics of shales and their rearrangement by compaction. *Sedimentology*, *15*(3–4), 247–260. https://doi.org/10.1111/j.1365-3091.1970.tb02188.x

Hoek, E., & Martin, C. D. (2014). Fracture initiation and propagation in intact rock—A review. *Journal of Rock Mechanics and Geotechnical Engineering*, *6*(4), 287–300. https://doi.org/10.1016/j.jrmge.2014.06.001

Kobchenko, M., Panahi, H., Renard, F., Dysthe, D., Malthe-Sorrenssen, A., Mazzini, A., et al. (2011). 4D imaging of fracturing in organic-rich shales during heating. *Journal of Geophysical Research*, *116*, B12201. https://doi.org/10.1029/2011JB008565

Kwon, O., Kronenberg, A. K., Gangi, A. F., & Johnson, B. (2001). Permeability of Wilcox shale and its effective pressure law. *Journal of Geophysical Research*, *106*(B9), 19,339–19,353. https://doi.org/10.1029/2001JB000273

Lash, G. G., & Engelder, T. (2005). An analysis of horizontal microcracking during catagenesis: Example from the Catskill delta complex. *AAPG Bulletin*, *89*(11), 1433–1449. https://doi.org/10.1306/05250504141

Lee, H., & Jeon, S. (2011). An experimental and numerical study of fracture coalescence in pre-cracked specimens under uniaxial compression. *International Journal of Solids and Structures*, *48*(6), 979–999. https://doi.org/10.1016/j.ijsolstr.2010.12.001

Lewan, M. D., & Roy, S. (2011). Role of water in hydrocarbon generation from Type-I kerogen in Mahogany oil shale of the Green River Formation. *Organic Geochemistry*, *42*(1), 31–41. https://doi.org/10.1016/j.orggeochem.2010.10.004

Lockner, D. A., Byerlee, J. D., Kuksenko, V., Ponomarev, A., & Sidorin, A. (1992). Observations of quasistatic fault growth from acoustic emissions. *International Geophysics*, *51*, 3–31. https://doi.org/10.1016/S0074-6142(08)62813-2

Louis, L., Wong, T. F., & Baud, P. (2007). Imaging strain localization by X-ray radiography and digital image correlation: Deformation bands in Rothbach sandstone. *Journal of Structural Geology*, *29*(1), 129–140. https://doi.org/10.1016/j.jsg.2006.07.015

Madden, E. H., Cooke, M. L., & McBeck, J. (2017). Energy budget and propagation of faults via shearing and opening using work optimization. *Journal of Geophysical Research: Solid Earth*, *122*, 6757–6772. https://doi.org/10.1002/2017JB014237

Meléndez-Martínez, J., & Schmitt, D. R. (2016). A comparative study of the anisotropic dynamic and static elastic moduli of unconventional reservoir shales: Implication for geomechanical investigations. *Geophysics*, *81*(3), D245–D261. https://doi.org/10.1190/geo2015-0427.1

Narr, W., & Suppe, J. (1991). Joint spacing in sedimentary rocks. *Journal of Structural Geology*, *13*(9), 1037–1048. https://doi.org/10.1016/0191-8141(91)90055-N

Ong, O. N., Schmitt, D. R., Kofman, R. S., & Haug, K. (2016). Static and dynamic pressure sensitivity anisotropy of a calcareous shale. *Geophysical Prospecting*, *64*(4), 875–897. https://doi.org/10.1111/1365-2478.12403

Panahi, H., Kobchenko, M., Renard, F., Mazzini, A., Scheibert, J., Dysthe, D., et al. (2013). 4D X-ray tomography imaging of hydrocarbon escape pathway formation in heated organic-rich shales: A proxy for primary migration? *SPE Journal*, SPE162939, *18*, 366–377.

Park, C. H., & Bobet, A. (2009). Crack coalescence in specimens with open and closed flaws: A comparison. *International Journal of Rock Mechanics and Mining Sciences*, *46*(5), 819–829. https://doi.org/10.1016/j.ijrmms.2009.02.006

Reches, Z. E., & Lockner, D. (1994). Nucleation and growth of faults in brittle rocks. *Journal of Geophysical Research*, *99*(B9), 18,159–18,173. https://doi.org/10.1029/94JB00115

Renard, F., Cordonnier, B., Dysthe, D., Boller, E., Tafforeau, P., & Rack, A. (2016). A deformation rig for synchrotron microtomography studies of geomaterials under conditions down to 10 km depth in the Earth. *Journal of Synchrotron Radiation*, *23*(4), 1030–1034. https://doi.org/10.1107/S1600577516008730

Renard, F., Cordonnier, B., Kobchenko, M., Kandula, N., Weiss, J., & Zhu, W. (2017). Microscale characterization of rupture nucleation unravels precursors to faulting in rocks. *Earth and Planetary Science Letters*, *476*, 69–78. https://doi.org/10.1016/j.epsl.2017.08.002

Renard, F., & McBeck, J. (2018). Investigating the onset of strain localization within anisotropic shale using digital volume correlation of time-resolved X-ray microtomography images (data set). *Norstore*. https://doi. org/10.11582/2018.00005

Sagong, M., & Bobet, A. (2002). Coalescence of multiple flaws in a rock-model material in uniaxial compression. *International Journal of Rock Mechanics and Mining Sciences*, *39*(2), 229–241. https://doi.org/10.1016/S1365-1609(02)00027-8

Sarout, J., & Guéguen, Y. (2008). Anisotropy of elastic wave velocities in deformed shales: Part 1—Experimental results. *Geophysics*, *73*(5), D75–D89. https://doi.org/10.1190/1.2952744

Scholz, C. H. (1968). Microfracturing and the inelastic deformation of rock in compression. *Journal of Geophysical Research*, *73*(4), 1417–1432. https://doi.org/10.1029/JB073i004p01417

Shen, B., Stephansson, O., Einstein, H. H., & Ghahreman, B. (1995). Coalescence of fractures under shear stress experiments. *Journal of Geophysical Research*, *100*(B4), 5975–5990. https://doi.org/10.1029/95JB00040

Sviridov, V. A., Mayr, S. I., & Shapiro, S. A. (2017). Elastic properties of two VTI shale samples as a function of uniaxial stress: Experimental results and application of the porosity-deformation approach. *Geophysics*, *82*(6), C201–C210. https://doi.org/10.1190/geo2016-0459.1

Tang, C. A., Lin, P., Wong, R. H. C., & Chau, K. T. (2001). Analysis of crack coalescence in rock-like materials containing three flaws—Part II: Numerical approach. *International Journal of Rock Mechanics and Mining Sciences*, *38*(7), 925–939. https://doi.org/10.1016/S1365-1609(01)00065-X

Tudisco, E., Andò, E., Cailletaud, R., & Hall, S. A. (2017). TomoWarp2: A local digital volume correlation code. *SoftwareX*, *6*, 267–270. https://doi.org/10.1016/j.softx.2017.10.002

Tudisco, E., Hall, S., Charalampidou, E., Kardjilov, N., Hilger, A., & Sone, H. (2015). Full-field measurements of strain localisation in sandstone by neutron tomography and 3D-volumetric digital image correlation. *Physics Procedia*, *69*, 509–515. https://doi.org/10.1016/j.phpro.2015.07.072

Vermilye, J. M., & Scholz, C. H. (1998). The process zone: A microstructural view of fault growth. *Journal of Geophysical Research*, *103*(B6), 12,223–12,237. https://doi.org/10.1029/98JB00957

Wong, L. N. Y., & Einstein, H. H. (2009). Crack coalescence in molded gypsum and Carrara marble: Part 1. Macroscopic observations and interpretation. *Rock Mechanics and Rock Engineering*, *42*(3), 475–511. https://doi.org/10.1007/s00603-008-0002-4

Wong, R. H. C., Chau, K. T., Tang, C. A., & Lin, P. (2001). Analysis of crack coalescence in rock-like materials containing three flaws—Part I: Experimental approach. *International Journal of Rock Mechanics and Mining Sciences*, *38*(7), 909–924. https://doi.org/10.1016/S1365-1609(01)00064-8

Zadeh, M. K., Mondol, N. H., & Jahren, J. (2016). Compaction and rock properties of Mesozoic and Cenozoic mudstones and shales, northern North Sea. *Marine and Petroleum Geology*, *76*, 344–361. https://doi.org/10.1016/j.marpetgeo.2016.05.024